Layered Materials

International Edition: DOI: 10.1002/anie.201508216
German Edition: DOI: 10.1002/ange.201508216

Fabrication of Two-Dimensional Lateral Heterostructures of WS_2/$WO_3 \cdot H_2O$ Through Selective Oxidation of Monolayer WS_2

Pengshang Zhou, Qun Xu, Hongxiang Li, Yun Wang,* Bo Yan, Yunchun Zhou, Jiafu Chen, Jianan Zhang, and Kaixi Wang*

Abstract: *Two-dimensional (2D) lateral heterostructures have emerged as a hot topic in the fast evolving field of advanced functional materials , but their fabrication is challenging. The layer-structured* WS_2 *was theoretically demonstrated to be inert to oxidation except for the monolayer, which can be selectively oxidized owing to the simultaneous interaction of oxygen with both sides. Combined with the theoretical calculations, a new method was developed for the successful construction of 2D lateral heterostructures of* $WS_2/WO_3 \cdot H_2O$ *in an ambient environment, based on a simple liquid-phase solution exfoliation. These lateral heterostructures of* $WS_2/WO_3 \cdot H_2O$ *have interesting properties, as indicated by enhanced photocatalytic activity toward the degradation of methyl orange (MO).*

In the wake of the discovery of graphene,[1] a vibrant research field has emerged around two-dimensional (2D) layered materials, a unique class of materials that are characterized by strong in-plane covalent bonding and weak non-covalent bonding between layers.[2] Individual, atomically thin layers arising from the successful exfoliation of 2D layered nanosheets can serve as building blocks for promising heteromaterials with either lateral or vertical 2D heterostructures. This approach has attracted great attention in terms of both fundamental studies and practical applications.[3] Most of the previous studies have focused on vertical heterostructures, which are held together by van der Waals forces, owing to their relative simplicity of fabrication. However, lateral heterostructures, with two materials linked by covalent bonds, may possess potential for the development of band-gap engineered applications such as electronics and photocatalysis.[4]

2D lateral heterostructures based on graphene and boron nitride (BN) were first synthesized by Levendorf et al. by using a helium-leak-checked semiconductor-grade tube furnace.[5] In 2014, fabrication of transition-metal dichalcogenides (TMDCs) was conducted by chemical vapor deposition (CVD).[6] The high cost resulting from the high temperature and clean environment required during the synthesis will limit the large-scale development of 2D lateral heterostructures. Therefore, the search of facile fabrication methods becomes imperative owing to the scientific interest and practical importance.

Liquid exfoliation is simple and can be used to produce most 2D layers.[7] Considering the possibility of chemical reactions in solution, there is more space to be explored in a liquid-phase solution-exfoliation strategy. Supercritical carbon dioxide (sc-CO_2) has been used to assist the exfoliation of layered materials,[8] owing to its excellent performance, for example, high diffusion coefficients, outstanding wetting of surfaces, and low interfacial tension.[9] In this work, we successfully exfoliated monolayer or few-layer WS_2 from bulk WS_2 with the assistance of sc-CO_2, and then partially converted them into tungsten oxide monohydrate ($WO_3 \cdot H_2O$) through oxidation. Finally, heterostructures of $WS_2/WO_3 \cdot H_2O$ were constructed.

The results obtained from scanning electron microscopy (SEM; Figure S1 in the Supporting Information), Raman spectroscopy (Figure S2), photoluminescence (PL) spectroscopy (Figure S3), and atomic force microscopy (AFM, Figure S4) confirmed the successful exfoliation of WS_2 nanosheets. Transmission electron microscopy (TEM) images and selected-area electron diffraction (SAED) analyses are given in Figure 1. The low-magnification TEM image (Figure 1 a) shows that the edge angle of the obtained nanosheets is 120°,

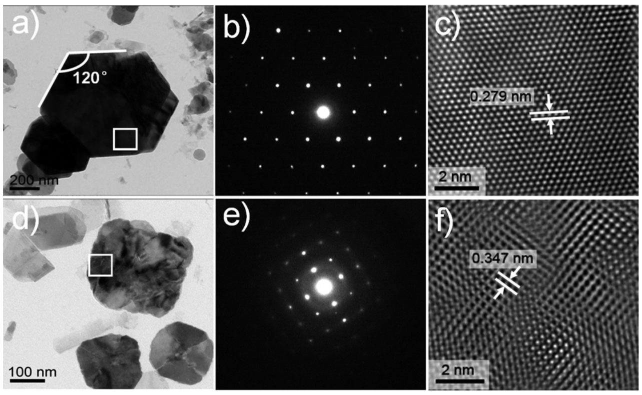

Figure 1. TEM images of the as-prepared nanosheets at 3000 rpm. a, d) Low-magnification TEM images of the nanosheets. b, e) SAED patterns of the region outlined by the squares in (a) and (d) respectively. c, f) Filtered images of part of the HRTEM images (see Figure S5 in the Supporting Information).

---

[*] P. Zhou, Prof. Q. Xu, H. Li, B. Yan, Dr. J. Chen, Dr. J. Zhang, K. Wang
College of Materials Science and Engineering, Zhengzhou University
Zhengzhou 450052 (China)
E-mail: qunxu@zzu.edu.cn

Dr. Y. Wang
Centre for Clean Environment and Energy and
Griffith School of Environment, Griffith University (Australia)
E-mail: yun.wang@griffith.edu.au

Dr. Y. Zhou
National Analytical Research Center of Electrochemistry and Spectroscopy, Changchun Institute of Applied Chemistry
Chinese Academy of Sciences, Changchun 130022 (China)

Supporting information for this article is available on the WWW under http://dx.doi.org/10.1002/anie.201508216.

thus suggesting that the nanosheets preserve the characteristic of WS_2 hexagonal structure. SAED (Figure 1 b) further confirms the hexagonal lattice structure. Figure 1 c presents a filtered image of the red region in Figure S5a. The atoms exhibit an obvious hexagonal atomic arrangement, with the spacing of adjacent lattices being 0.279 nm, which is in good agreement with the typical (100) plane of pristine 2H-WS_2.[10] Of note, there are nanosheets with orthorhombic crystal structures (Figure S5b), as highlighted by the SAED pattern (Figure 1 e). The filtered image enclosed by the yellow square in Figure S5b is shown in Figure 1 f, which clearly shows that the lattice structure is consistent with $WO_3{\cdot}H_2O$.[11] As shown in Figure 1 d, non-uniform contrast in the low TEM image suggests some defects on the surface of the nanosheets, presumably caused by an inhomogeneous dehydration process in $WO_3{\cdot}H_2O$ structure.[11c] Alternatively, the lattice spacing of 0.347 nm is assigned to the (111) plane of $WO_3{\cdot}H_2O$. All these characterization results indicate the coexistence of WS_2 and $WO_3{\cdot}H_2O$ in our devised reaction system. Furthermore, we performed energy-dispersive spectroscopy (EDS) analysis on the obtained nanosheets at 3000 rpm (Figure S6). As expected, the measured molar ratio of W/S is higher than the stoichiometric ratio of WS_2, thus further indicating that another W phase exists in the nanosheets.

The crystal structures and the possible phase change of the as-prepared nanosheets were examined by X-ray diffraction (XRD, Figure 2 a) studies. Bulk WS_2 can be well indexed into the well-known 2H-WS_2. The sample obtained at 3000 rpm exhibits all characteristic diffraction peaks corresponding to 2H-WS_2, thus indicating that the crystal structure of 2H-WS_2 is preserved during exfoliation. A striking feature in the patterns is that two new peaks appear at the $2\theta = 23.826°$ and 25.704°, which are attributed to orthorhombic $WO_3{\cdot}H_2O$ (PDF card no. 43-0679, space group *Pmnb*, No. 62), which is consistent with the SAED pattern (Figure 1 e) and the lattice shown in Figure 1 f.

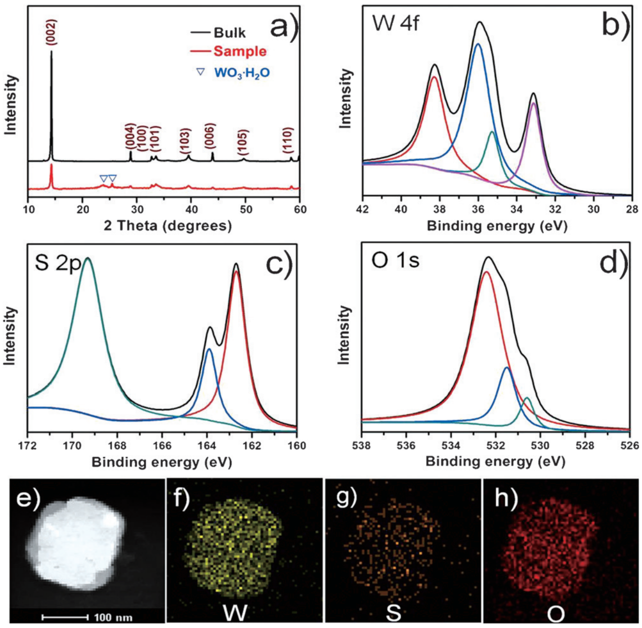

Figure 2. a) XRD patterns of bulk WS_2 (black) and the sample nanosheets (red). b–d) High-resolution XPS of the as-obtained nanosheets at binding energies corresponding to W 4f, S 2p, and O 1 s, respectively. e–h) STEM image and corresponding elemental mapping images.

To further investigate the chemical composition, X-ray photoelectron spectroscopy (XPS) and elemental mapping imaging were performed. As shown in Figure 2 b, peaks located at 33.10 and 35.23 eV are ascribed to W $4f_{7/2}$, W $4f_{5/2}$ lines of the W atoms in a $+4$ form.[10] The higher energies of 36.07 and 38.30 eV correspond to W $4f_{5/2}$ and W $4f_{7/2}$ peaks of the atoms in an oxidation state of $+6$, which agrees well with the range of values reported for WO_3.[12] The XPS data for S is shown in Figure 2 c: three components at 162.69, 163.9, and 169.3 eV are observed after curve fitting. The peaks at 162.69 and 163.9 eV can be attributed to S $2p_{3/2}$ and S $2p_{1/2}$ orbitals of divalent sulfide ions, respectively.[13] The third peak at 169.3 eV can be assigned to $+6$ S, which comes from the oxidation of divalent sulfide ions. Meanwhile, the XPS for O 1s was also carried out in our study (Figure 2 d). A binding energy of 530.6 eV indicates the existence of oxygen bonded to hexavalent tungsten in $WO_3{\cdot}H_2O$.[11c,14] The signal at 531.5 eV is related to the −OH bond on the sample. The OH group can come from from surface-adsorbed or interstructure water molecules inside the $WO_3{\cdot}H_2O$.[15] Apart from the two peaks, a new peak appears at 532.4 eV, which can be attributed to nonstoichometric tungsten oxides.[14b] A scanning transmission electron microscope (STEM) image and the corresponding elemental mapping images (Figure 2 e–h) clearly reveal the homogeneous distribution of W, S, and O atoms over the entire nanosheets. This experimental observation is consistent with the HRTEM and EDS analyses, which unambiguously indicate that the obtained nanosheets contain heterostructures of WS_2 and $WO_3{\cdot}H_2O$.

It is well known that much smaller flakes can be obtained by centrifuging at higher rates.[16] We thus prepared smaller nanosheets by increasing the centrifugation sequentially rate from 3000 rpm to 12 000 rpm. HRTEM was performed to confirm the phase composition and crystallinity of the samples. The nanosheets obtained at 9000 rpm display lattice types covering both the typical 2H-WS_2 and orthorhombic $WO_3{\cdot}H_2O$. Elemental mapping images further demonstrate the formation of heterostructures (Figure S7). HRTEM of the sample obtained at 12 000 rpm is depicted in Figure 3. The insets in Figure 3 a show schematic structures of the unit cells of $WO_3{\cdot}H_2O$ and 2H-WS_2. 2H-WS_2 exhibits hexagonal closed packing and trigonal prismatic coordination, wherein a plane of W atoms is sandwiched covalently between two planes of S atoms, while the unit cell of $WO_3{\cdot}H_2O$ is a WO_6 octahedron. The filtered images (Figure 3 b and c) and the corresponding FFT illustrate the two lattice types more intuitively. The presence of uncertain lattice types between the two phases can be assigned to the transition from 2H-WS_2 to $WO_3{\cdot}H_2O$.

On the basis of the characterization, we propose a mechanism for the formation of WS_2/$WO_3{\cdot}H_2O$ heterostructures. First, sc-CO_2 can permeate easily between WS_2 layers to expand the interlayer distance, which is beneficial for the exfoliation of WS_2. Then single and few-layer WS_2 nanosheets are obtained (Figure 4 a), and more importantly, more active

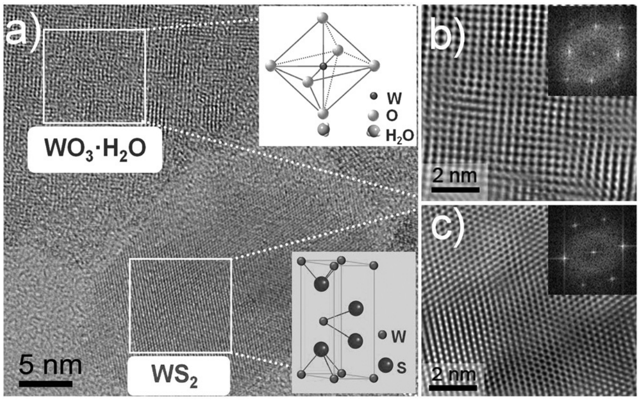

Figure 3. TEM images of the $WS_2/WO_3 \cdot H_2O$ nanosheets prepared at 12000 rpm. a) HRTEM image. Inset: schematic structures of the unit cells of $WO_3 \cdot H_2O$ and 2H-WS_2. b, c) Filtered images enclosed by the two squares in (a), respectively. Inset: the corresponding FFT.

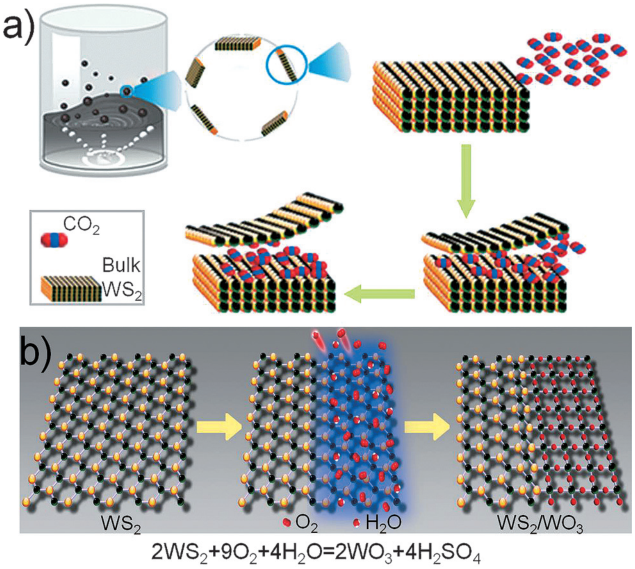

Figure 4. Schematic illustration of the fabrication of the $WS_2/WO_3 \cdot H_2O$ heterostructures. a) The exfoliation process. b) Partial oxidation.

edges, which are beneficial for the further oxidation of WS_2 can be exposed. Previous theoretical studies have demonstrated that the electronic structures of monolayer WS_2 are very different from multilayer ones as a consequence of the missing interlayer interactions.[17] This raises the question of whether the chemical reactivities of WS_2 with monolayer or multilayer structures are also different. To answer this question, the adsorption properties of O_2 on the top side of monolayer and bilayer WS_2 were studied theoretically by using density functional theory (DFT) with the consideration of the van der Waals forces.[18,19] It was found that the adsorption properties are almost identical, and the dissociative adsorption is energetically preferred, with adsorption energies of -0.374 and -0.377 eV for the monolayer and bilayer models, respectively (Figure S8). Further calculation indicates that molecular adsorption with two O atoms bonded to one S atom for the bilayer model is unfavorable, with the adsorption energy being $+0.2$ eV. While the specific structure of the monolayer WS_2 allows oxygen to be adsorbed on both sides simultaneously. When one O atom is adsorbed on one side of the WS_2 monolayer, molecular adsorption becomes energetically preferred, with the adsorption energy of -0.24 eV/O_2. This demonstrates that the chemical properties of the monolayer are through the synergetic interaction of adsorbents of oxygen atoms on both sides. Meanwhile, our calculations indicate that the produced SO_2 group can be further oxidized by O_2 to form SO_3, with one surface oxygen atom formed by substituting a surface sulfur atom (Figure S9). The strong reaction energy of -4.92 eV/O_2 suggests that such surface substitution is thermodynamically preferred. Therefore, monolayer WS_2 can be oxidized into oxides, while the multilayer WS_2 remains intact during the reaction, i.e., the 2D lateral heterostructures can be produced only when the WS_2 is a single layer, as illustrated in Figure 4b.

The photodegradation of MO was chosen as a probe reaction to evaluate the photocatalytic activity of the as-prepared $WS_2/WO_3 \cdot H_2O$ heterostructures. As can be seen from Figure 5a, the MO solution could be degraded by 90% in 40 min under UV irradiation, while under visible-light irradiation, more than 90% of the MO was degraded in 240 min. The degradation rates under both UV and visible light are higher than those with bulk WS_2 (Figure S10c). To explain the enhancement of the photocatalytic properties of the heterostructures, we explored the photoelectrochemical (PEC) behavior of the sample and bulk WS_2. The $WS_2/WO_3 \cdot H_2O$ electrode displays photocurrent response of 6×10^{-5} A cm^{-2} under visible irradiation, which is two times higher than that of bulk WS_2 (Figure 5b). The enhanced photocurrent response is closely related to the creation of $WS_2/WO_3 \cdot H_2O$ heterostructures. As shown in *Figure* 5c, the potential of WS_2 at the conduction band (CB) minimum is

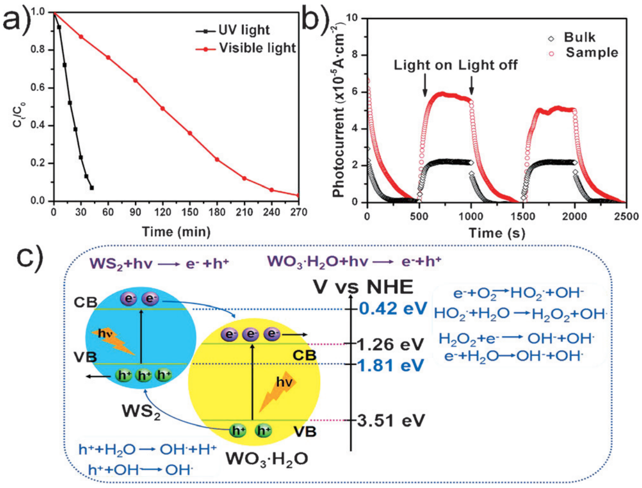

Figure 5. a) Photocatalytic degradation of MO solutions in the presence of the nanosheets. b) The photocurrent response (-0.3 V bias) of the sample nanosheets and bulk WS_2 in 1 м H_2SO_4 electrolyte under visible light. c) Schematic diagram of charge transfer in the $WS_2/WO_3 \cdot H_2O$ heterostructures under visible light.

0.42 eV vs. the normal hydrogen electrode (NHE), which is lower than that of $WO_3{\cdot}H_2O$ (1.26 eV),[10,20] so electrons in the CB of WS_2 can be transferred to that of $WO_3{\cdot}H_2O$ under visible excitation. Furthermore, since the valence band (VB) maximum level of $WO_3{\cdot}H_2O$ is 3.51 eV, which is higher than that of WS_2 (1.81 eV), holes in the VB of $WO_3{\cdot}H_2O$ can be transferred in the opposite direction. In the end, plenty of electrons and holes are found on the surface of $WO_3{\cdot}H_2O$ and WS_2, respectively. All-round efficient charge separation is thus realized.

In summary, we have demonstrated that 2D lateral WS_2/$WO_3{\cdot}H_2O$ heterostructures can be fabricated with the assistance of sc-CO_2 since only monolayer WS_2 is likely to be oxidized based on our first-principles theoretical results. The presence of heterostructures allows for long-lived electron-hole pairs, thus resulting in enhanced photocatalytic activity toward the degradation of MO and higher photocurrent under visible-light irradiation. Therefore, the facile preparation method developed herein provides a general method for obtaining photocatalytic semiconductor hybrid nanostructured materials, and it is anticipated that this method could be extended to the preparation of other high qualified heterostructures.

Acknowledgements

We are grateful for the National Natural Science Foundation of China (Nos. 51173170, 21101141), financial support from the Innovation Talents Award of Henan Province (114200510019), and the Key program of science and technology (121PZDGG213) from Zhengzhou Bureau of science and technology. This research was undertaken on the National Computational Infrastructure (NCI) in Canberra, Australia.

Keywords: heterostructures · nanosheets · photocatalysis · tungsten oxides · tungsten sulfides

How to cite: *Angew. Chem. Int. Ed.* **2015**, *54*, 15226–15230
Angew. Chem. **2015**, *127*, 15441–15445

---

[1] K. S. Novoselov, A. K. Geim, S. V. Morosov, D. Jiang, Y. Zhang, S. V. Dubonos, I. V. Grigorieva, A. A. Firsov, *Science* **2004**, *306*, 666–669.

[2] a) S. Z. Butler, S. M. Hollen, L. Cao, Y. Cui, J. A. Gupta, H. R. Gutierrez, T. F. Heinz, S. S. Hong, J. Huang, A. F. Ismach, E. Johnston-Halperin, M. Kuno, V. V. Plashnitsa, R. D. Robinson, R. S. Ruoff, S. Salahuddin, J. Shan, L. Shi, M. G. Spencer, M. Terrones, W. Windl, J. E. Goldberger, *ACS Nano* **2013**, *7*, 2898–2926; b) K. S. Novoselov, D. Jiang, F. Schedin, T. J. Booth, V. V. Khotkevich, S. V. Morozov, A. K. Geim, *Proc. Natl. Acad. Sci. USA* **2005**, *102*, 10451–10453.

[3] a) Q. H. Wang, K. Kalantar-Zadeh, A. Kis, J. N. Coleman, M. S. Strano, *Nat. Nanotechnol.* **2012**, *7*, 699–712; b) M. Xu, T. Liang, M. Shi, H. Chen, *Chem. Rev.* **2013**, *113*, 3766–3798; c) D. Jariwala, V. K. Sangwan, L. J. Lauhon, T. J. Marks, M. C. Hersam, *ACS Nano* **2014**, *8*, 1102–1120; d) M. Chhowalla, H. S. Shin, G. Eda, L.-J. Li, K. P. Loh, H. Zhang, *Nat. Chem.* **2013**, *5*, 263–275; e) C.-H. Lee, A. M. van der Zander, W. Chen, Y. Li, M. Han, X. Cui, G. Arefe, C. Nuckolls, T. F. Heinz, J. Guo, J. Hone, P. Kim, *Nat. Nanotechnol.* **2014**, *9*, 676–681; f) M. M. Furchi, A. Pospischil, F. Libsch, J. Burgdörfer, T. Mueller, *Nano Lett.* **2014**, *14*, 4785–4791; g) X. Hong, J. Kim, S.-F. Shi, Y. Zhang, C. Jin, Y. Sun, S. Tongay, J. Wu, Y. Zhang, F. Wang, *Nat. Nanotechnol.* **2014**, *9*, 682–686; h) R. Cheng, D. Li, H. Zhou, C. Wang, A. Yin, S. Jiang, Y. Liu, Y. Chen, Y. Huang, X. Duan, *Nano Lett.* **2014**, *14*, 5590–5597; i) A. K. Geim, I. V. Grigorieva, *Nature* **2013**, *499*, 419–425; j) A. Pospischil, M. M. Furchi, T. Mueller, *Nat. Nanotechnol.* **2014**, *9*, 257–261; k) B. W. Baugher, H. O. Churchill, Y. Yang, P. Jarillo-Herrero, *Nat. Nanotechnol.* **2014**, *9*, 262–267; l) C. Tan, H. Zhang, *Chem. Soc. Rev.* **2015**, *44*, 2713–2731; m) H. Li, J. Wu, Z. Yin, H. Zhang, *Acc. Chem. Res.* **2014**, *47*, 1067–1075; n) S. Tang, H. Wang, Y. Zhang, A. Li, H. Xie, X. Liu, L. Liu, T. Li, F. Huang, X. Xie, M. Jiang, *Sci. Rep.* **2013**, *3*, 2666; o) Y. Jung, J. Shen, Y. Sun, J. J. Cha, *ACS Nano* **2014**, *8*, 9550–9557; p) X. Huang, C. Tan, Z. Yin, H. Zhang, *Adv. Mater.* **2014**, *26*, 2185–2204; q) X. Huang, Z. Zeng, H. Zhang, *Chem. Soc. Rev.* **2013**, *42*, 1934–1946; r) Z. Zeng, Z. Yin, X. Huang, H. Li, Q. He, G. Lu, F. Boey, H. Zhang, *Angew. Chem. Int. Ed.* **2011**, *50*, 11093–11097; *Angew. Chem.* **2011**, *123*, 11289–11293; s) Z. Zeng, T. Sun, J. Zhu, X. Huang, Z. Yin, G. Lu, Z. Fan, Q. Yan, H. H. Hug, H. Zhang, *Angew. Chem. Int. Ed.* **2012**, *51*, 9052–9056; *Angew. Chem.* **2012**, *124*, 9186–9190; t) Z. Yin, X. Zhang, Y. Cai, J. Chen, J. Wong, Y.-Y. Tay, J. Chai, J. Wu, Z. Zeng, B. Zheng, H. Y. Yang, H. Zhang, *Angew. Chem. Int. Ed.* **2014**, *53*, 12560–12565; *Angew. Chem.* **2014**, *126*, 12768–12773.

[4] C. Huang, S. Wu, A. M. Sanchez, J. J. Peters, R. Beanland, J. S. Ross, P. Yao, W. Rivera, D. H. Cobden, X. Xu, *Nat. Mater.* **2014**, *13*, 1096–1101.

[5] M. P. Levendorf, C.-J. Kim, L. Brown, P. Y. Huang, R. W. Havener, D. A. Muller, J. Park, *Nature* **2012**, *488*, 627–632.

[6] a) Y. Gong, J. Lin, X. Wang, G. Shi, S. Lei, Z. Lin, X. Zou, G. Ye, R. Vajtai, B. I. Yakobson, H. Terrones, M. Terrones, B. K. Tay, J. Lou, S. T. Pantelides, Z. Liu, W. Zhou, P. M. Ajayan, *Nat. Mater.* **2014**, *13*, 1135–1142; b) X. Duan, C. Wang, J. C. Shaw, R. Cheng, Y. Chen, H. Li, X. Wu, Y. Tang, Q. Zhang, A. Pan, J. Jiang, R. Yu, Y. Huang, X. Duan, *Nat. Nanotechnol.* **2014**, *9*, 1024–1030.

[7] a) P. Blake, P. D. Brimicombe, R. R. Nair, T. J. Booth, D. Jiang, F. Schedin, K. S. Novoselov, *Nano Lett.* **2008**, *8*, 1704–1708; b) Y. Hernandez, V. Nicolosi, M. Lotya, F. M. Blighe, Z. Sun, S. De, J. N. Coleman, *Nat. Nanotechnol.* **2008**, *3*, 563–568; c) J. N. Coleman, M. Lotya, A. O'Neill, S. D. Bergin, P. J. King, U. Khan, K. Young, A. Gaucher, S. De, R. J. Smith, L. V. Shvets, S. K. Arora, G. Stanton, H.-Y. Kim, K. Lee, G. T. Kim, G. S. Duesberg, T. Hallam, J. J. Boland, J. Wang, J. F. Donegan, G. C. Grunlan, G. Moriarty, A. Shmeliov, R. J. Nicholls, *Science* **2011**, *331*, 568–571.

[8] a) D. Rangappa, K. Sone, M. S. Wang, U. K. Gautam, D. Golberg, H. Itoh, M. Ichihara, I. Honma, *Chem. Eur. J.* **2010**, *16*, 6488–6494; b) S. Xu, Q. Xu, N. Wang, Z. Chen, Q. Tian, H. Yang, K. Wang, *Chem. Mater.* **2015**, *27*, 3262–3272.

[9] K. P. Johnston, K. L. Harrison, M. J. Clarke, S. M. Howdle, M. P. Heitz, F. V. Bright, C. T. Carlier, W. Randolph, *Science* **1996**, *271*, 624–626.

[10] Y. Sang, Z. Zhao, M. Zhao, P. Hao, Y. Leng, H. Liu, *Adv. Mater.* **2015**, *27*, 363–369.

[11] a) W. Li, P. Da, Y. Zhang, Y. Wang, X. Lin, X. Gong, G. Zheng, *ACS Nano* **2014**, *8*, 11770–11777; b) M. Seifollahi Bazarjani, M. Hojamberdiev, K. Morita, G. Zhu, G. Cherkashinin, C. Fasel, T. Herrmann, H. Breitzke, A. Gurlo, R. Riedel, *J. Am. Chem. Soc.* **2013**, *135*, 4467–4475; c) J. Y. Zheng, G. Song, J. Hong, T. K. Van, A. U. Pawar, D. Y. Kim, C. W. Kim, Z. Haider, Y. S. Kang, *Cryst. Growth Des.* **2014**, *14*, 6057–6066.

[12] a) M. Epifani, E. Comini, R. Díaz, T. Andreu, A. Genc, J. Arbiol, P. Siciliano, G. Faglia, J. R. Morante, *ACS Appl. Mater. Interfaces* **2014**, *6*, 16808–16816; b) F. Y. Xie, L. Gong, X. Liu, Y. T. Tao,

W. H. Zhang, S. H. Chen, H. Meng, J. Chen, *J. Electron Spectrosc. Relat. Phenom.* **2012**, *185*, 112 – 118.

[13] D. Voiry, H. Yamaguchi, J. Li, R. Silva, D. C. B. Alves, T. Fujita, M. W. Chen, T. Asefa, V. B. Shenoy, G. Eda, M. Chhowalla, *Nat. Mater.* **2013**, *12*, 850 – 855.

[14] a) F. S. Manciu, J. L. Enriquez, W. G. Durrer, Y. Yun, C. V. Ramana, S. K. Gullapalli, *J. Mater. Res.* **2010**, *25*, 2401 – 2406; b) A. Lewera, L. Timperman, A. Roguska, N. Alonso-Vante, *J. Phys. Chem. C* **2011**, *115*, 20153 – 20159.

[15] H. S. Shim, J. W. Kim, Y. E. Sung, W. B. Kim, *Sol. Energy Mater. Sol. Cells* **2009**, *93*, 2062 – 2068.

[16] D. Hanlon, C. Backes, T. M. Higgins, M. Hughes, A. O'Neill, P. King, N. McEvoy, G. S. Duesberg, B. M. Sanchez, H. Pettersson, V. Nicolosi, J. N. Coleman, *Chem. Mater.* **2014**, *26*, 1751 – 1763.

[17] Y. Leng, S. Jiang, *Phys. Rev. B* **2001**, *64*, 115415.

[18] G. Kresse, J. Hafner, *Phys. Rev. B* **1993**, *47*, 558.

[19] T. Bučko, S. Lebègue, J. G. Ángyán, J. Hafner, *J. Chem. Phys.* **2014**, *141*, 034114.

[20] S. Guo, M. Zhen, M. Sun, X. Zhang, Y. Zhao, L. Liu, *RSC Adv.* **2015**, *5*, 16376 – 16385.

Received: September 2, 2015
Revised: September 30, 2015